A MEEVC discretization for two-dimensional incompressible Navier-Stokes equations with general boundary conditions

Zhang, Yi; Palha, Artur; Gerritsma, Marc; Yao, Qinghe

DOI
10.1016/j.jcp.2024.113080

Publication date
2024

Document Version
Final published version

Published in
Journal of Computational Physics

Citation (APA)
Zhang, Y., Palha, A., Gerritsma, M., & Yao, Q. (2024). A MEEVC discretization for two-dimensional incompressible Navier-Stokes equations with general boundary conditions. *Journal of Computational Physics*, *510*, Article 113080. https://doi.org/10.1016/j.jcp.2024.113080

Journal of Computational Physics 510 (2024) 113080

Contents lists available at ScienceDirect

Journal of Computational Physics

journal homepage: www.elsevier.com/locate/jcp

A MEEVC discretization for two-dimensional incompressible Navier-Stokes equations with general boundary conditions

Yi Zhang [a,*], Artur Palha [b], Marc Gerritsma [c], Qinghe Yao [d]

[a] Guilin University of Electronic Technology, School of Mathematics and Computing Science, Guilin, China
[b] Delft University of Technology, Delft Institute of Applied Mathematics, Delft, the Netherlands
[c] Delft University of Technology, Faculty of Aerospace Engineering, Delft, the Netherlands
[d] Sun Yat-sen University, School of Aeronautics and Astronautics, Shenzhen, China

ARTICLE INFO

Keywords:
Navier-Stokes equations
de Rham complex
Structure-preserving discretization
No-slip boundary condition

ABSTRACT

In this work, we present a mass, energy, enstrophy and vorticity conserving (MEEVC) mixed finite element discretization for two-dimensional incompressible Navier-Stokes equations as an alternative to the original MEEVC scheme proposed in A. Palha and M. Gerritsma (2017) [5]. The present method can incorporate general boundary conditions. Conservation properties are proven. Supportive numerical experiments with both exact and inexact quadrature are provided.

1. Introduction

We consider the dimensionless rotational or Lamb form of two-dimensional incompressible (or, more strictly speaking, constant density) Navier-Stokes equations in a space-time domain, see for example [1–3],

$$\partial_t \boldsymbol{u} + \omega \times \boldsymbol{u} + \mathrm{Re}^{-1} \nabla \times \omega + \nabla P = \boldsymbol{f} \qquad \text{in } \Omega \times (0, T], \tag{1a}$$

$$\omega - \nabla \times \boldsymbol{u} = \boldsymbol{0} \qquad \text{in } \Omega \times (0, T], \tag{1b}$$

$$\nabla \cdot \boldsymbol{u} = 0 \qquad \text{in } \Omega \times (0, T], \tag{1c}$$

where $\Omega \subset \mathbb{R}^2$, is a bounded, contractible domain with a Lipschitz boundary $\partial\Omega$, $\partial_t := \frac{\partial}{\partial t}$, $\boldsymbol{u}$ is the velocity field, ω is the vorticity field, $P := p + \frac{1}{2}\boldsymbol{u} \cdot \boldsymbol{u}$ is the total pressure (with p being the static pressure), $\boldsymbol{f}$ is the external (body) force, and Re denotes the Reynolds number. (1) is supplemented with an initial condition,

$$\boldsymbol{u}^0 = \boldsymbol{u}(\boldsymbol{x}, t_0), \tag{2}$$

and two pairs of boundary conditions,

* Corresponding author.
E-mail addresses: zhangyi_aero@hotmail.com (Y. Zhang), a.palha@tudelft.nl (A. Palha), m.i.gerritsma@tudelft.nl (M. Gerritsma), yaoqhe@sysu.edu.cn (Q. Yao).

https://doi.org/10.1016/j.jcp.2024.113080
Received 16 July 2023; Received in revised form 2 April 2024; Accepted 2 May 2024

Available online 8 May 2024

$$\begin{cases} \boldsymbol{u}\cdot\boldsymbol{n} = \widehat{u}_{\perp} & \text{on } \Gamma_{\perp}\times(0,T] \\ P = \widehat{P} & \text{on } \Gamma_{\widehat{P}}\times(0,T] \end{cases}, \quad \begin{cases} \omega = \widehat{\omega} & \text{on } \Gamma_{\widehat{\omega}}\times(0,T] \\ \boldsymbol{u}\times\boldsymbol{n} = \widehat{u}_{\parallel} & \text{on } \Gamma_{\parallel}\times(0,T] \end{cases}, \tag{3}$$

where $\boldsymbol{n}$ is the unit outward norm vector. In each pair, the boundary sections are disjoint; the boundary conditions are not active at the same boundary section, i.e., $\Gamma_{\perp}\cap\Gamma_{\widehat{P}} = \Gamma_{\widehat{\omega}}\cap\Gamma_{\parallel} = \emptyset$, and each pair is active over the whole boundary, $\Gamma_{\perp}\cup\Gamma_{\widehat{P}} = \Gamma_{\widehat{\omega}}\cup\Gamma_{\parallel} = \partial\Omega$, also see [4, Table 1]. Note that, when $\Gamma_{\widehat{P}} = \emptyset$, there is a singular mode in the total pressure of (1); the total pressure is determined up to a constant.

Recall that we have assumed constant density. The divergence free condition of velocity, (1c), then implies mass conservation. For two-dimensional incompressible flows, integral quantities of interest include

$$\begin{aligned} \textit{total kinetic energy (or simply energy)}\ \mathcal{K} &:= \frac{1}{2}\int_{\Omega} \boldsymbol{u}\cdot\boldsymbol{u}\ \mathrm{d}\Omega, \\ \textit{total enstrophy (or simply enstrophy)}\ \mathcal{E} &:= \frac{1}{2}\int_{\Omega} \omega\cdot\omega\ \mathrm{d}\Omega, \\ \textit{total palinstrophy (or simply palinstrophy)}\ \mathcal{P} &:= \frac{1}{2}\int_{\Omega} (\nabla\times\omega)\cdot(\nabla\times\omega)\ \mathrm{d}\Omega. \end{aligned}$$

In the absence of external body force,[1] i.e., $\boldsymbol{f} = \boldsymbol{0}$, and if there is no net flux of energy and enstrophy over the domain boundary, two-dimensional incompressible flows dissipate energy at a rate,

$$\partial_t \mathcal{K} = -2\mathrm{Re}^{-1}\mathcal{E}, \tag{4}$$

and, additionally dissipate enstrophy at a rate,

$$\partial_t \mathcal{E} = -2\mathrm{Re}^{-1}\mathcal{P}. \tag{5}$$

Furthermore, if the two-dimensional incompressible flow is in the inviscid limit ($\mathrm{Re}\to\infty$), namely, the flow is ideal, from (4) and (5), it conserves energy and enstrophy over time [5]. And the relation (1b) implies

$$\mathcal{W} := \int_{\Omega} \omega\ \mathrm{d}\Omega = \oint_{\partial\Omega} \boldsymbol{u}\times\boldsymbol{n}\ \mathrm{d}\Gamma, \tag{6}$$

where $\mathcal{W}$ is called the total vorticity. (6) shows that the total vorticity no matter whether the flow is ideal or not, is a conserved quantity over time provided $\oint_{\partial\Omega}\boldsymbol{u}\times\boldsymbol{n}\ \mathrm{d}\Gamma$ is not time dependent.

The first scheme that is mass, energy, enstrophy and vorticity conserving (MEEVC) was proposed in [5] where two evolution equations for velocity and vorticity are employed. The two evolution equations are staggered in time such that information can be transferred between each other through a midpoint temporal discretization scheme. As a result, both equations are linearized and the unknowns are decoupled to separate time instant sequences, which significantly lowers the computational cost. A drawback of this scheme is that the inclusion of no-slip boundary conditions requires indirect approaches and the suggested approach destroys the vorticity conservation property [6].

Olshanskii and Rebholz have discussed the role of adjoint discrete vorticity for structure preservation in their work [7]. For examples of mass and energy conserving scheme for incompressible flows, we refer to the work of Hanot [8], Schroeder et al. [9] and Evans and Hughes [10]. An extensive literature study on structure-preserving methods is given in [5]. For a more recent summary on structure-preserving methods for incompressible flows, we refer to, for example, [11]. And a comprehensive introduction to the mixed finite element method is given in the book of Boffi, Brezzi and Fortin [12].

In this work, we present a mixed high-order finite element discretization of two-dimensional incompressible Navier-Stokes equations that is also MEEVC, can incorporate general boundary conditions but avoids the evolution equation for vorticity. The functional setting will be given in Section 2. In Section 3, properties of the formulation are analyzed, which is followed by the introduction of the temporal discretization in Section 4. Numerical tests are presented in Section 5. Finally, conclusions are drawn in Section 6.

[1] Or when the external body force is conservative.

2. The mixed weak formulation

2.1. A brief introduction to function spaces employed

The space of square integrable functions, is

$$L^2(\Omega) := \left\{ f \mid \langle f, f \rangle_\Omega < +\infty \right\},$$

where $\langle \cdot, \cdot \rangle_\Omega$ denotes the L^2-inner product (or simply inner product) over the domain Ω. In $\mathbb{R}^2$, we will also use Sobolev spaces

$$H(\mathrm{curl};\Omega) := \left\{ \omega \,\middle|\, \omega \in L^2(\Omega),\ \nabla \times \omega \in \left[L^2(\Omega)\right]^2 \right\},$$
$$H(\mathrm{div};\Omega) := \left\{ \boldsymbol{u} \,\middle|\, \boldsymbol{u} \in \left[L^2(\Omega)\right]^2,\ \nabla \cdot \boldsymbol{u} \in L^2(\Omega) \right\},$$
$$H^1(\Omega) := \left\{ \phi \,\middle|\, \phi \in L^2(\Omega),\ \nabla \phi \in \left[L^2(\Omega)\right]^2 \right\},$$
$$H(\mathrm{rot};\Omega) := \left\{ \boldsymbol{\sigma} \,\middle|\, \boldsymbol{\sigma} \in \left[L^2(\Omega)\right]^2,\ \nabla \times \boldsymbol{\sigma} \in L^2(\Omega) \right\}.$$

They form two de Rham complexes [13] in two dimensions written as

$$\mathbb{R} \hookrightarrow H(\mathrm{curl};\Omega) \xrightarrow{\nabla\times} H(\mathrm{div};\Omega) \xrightarrow{\nabla\cdot} L^2(\Omega) \to 0, \tag{7}$$
$$\mathbb{R} \hookrightarrow H^1(\Omega) \xrightarrow{\nabla} H(\mathrm{rot};\Omega) \xrightarrow{\nabla\times} L^2(\Omega) \to 0. \tag{8}$$

In $\mathbb{R}^2$, $H(\mathrm{curl};\Omega)$ and $H^1(\Omega)$ are the same space at the continuous level. Two notations are used to indicate in which de Rham complex, i.e. (7) or (8), they play a role. Also see (1) and (2) of [14]. The trace operator, denoted by $\mathcal{T}$, restricts a function to a boundary section, $\Gamma \subseteq \partial\Omega$. The trace operator acting on $\omega \in H(\mathrm{curl};\Omega)$, $\phi \in H^1(\Omega)$, $\boldsymbol{u} \in H(\mathrm{div};\Omega)$ and $\boldsymbol{\sigma} \in H(\mathrm{rot};\Omega)$ is, respectively,

$$\mathcal{T}\omega = \omega|_\Gamma, \quad \mathcal{T}\phi = \phi|_\Gamma,$$
$$\mathcal{T}\boldsymbol{u} = \boldsymbol{u} \cdot \boldsymbol{n}|_\Gamma, \quad \mathcal{T}\boldsymbol{\sigma} = \boldsymbol{\sigma} \times \boldsymbol{n}|_\Gamma.$$

The trace spaces are

$$\mathcal{T}H(\mathrm{curl};\Omega,\Gamma) := \{ \mathcal{T}\omega \mid \omega \in H(\mathrm{curl};\Omega) \},$$
$$\mathcal{T}H(\mathrm{div};\Omega,\Gamma) := \{ \mathcal{T}\boldsymbol{u} \mid \boldsymbol{u} \in H(\mathrm{div};\Omega) \},$$
$$H^{1/2}(\Omega,\Gamma) := \left\{ \mathcal{T}\phi \mid \phi \in H^1(\Omega) \right\},$$
$$\mathcal{T}H(\mathrm{rot};\Omega,\Gamma) := \{ \mathcal{T}\boldsymbol{\sigma} \mid \boldsymbol{\sigma} \in H(\mathrm{rot};\Omega) \}.$$

For a complete introduction on Sobolev spaces, we refer to [15].

We use notations $C(\Omega)$, $D(\Omega)$, $G(\Omega)$, $R(\Omega)$ and $S(\Omega)$ to express finite dimensional conforming function spaces which are subsets of Sobolev spaces, i.e.,

$$C(\Omega) \subset H(\mathrm{curl};\Omega), \quad D(\Omega) \subset H(\mathrm{div};\Omega), \quad S(\Omega) \subset L^2(\Omega),$$
$$G(\Omega) \subset H^1(\Omega), \quad R(\Omega) \subset H(\mathrm{rot};\Omega),$$

and form discrete de Rham complexes in two-dimensional space,

$$\mathbb{R} \hookrightarrow C(\Omega) \xrightarrow{\nabla\times} D(\Omega) \xrightarrow{\nabla\cdot} S(\Omega) \to 0, \tag{9}$$
$$\mathbb{R} \hookrightarrow G(\Omega) \xrightarrow{\nabla} R(\Omega) \xrightarrow{\nabla\times} S(\Omega) \to 0.$$

Note that, although $H(\mathrm{curl};\Omega)$ and $H^1(\Omega)$ indicate the same space at the continuous level, their discrete counterparts, $C(\Omega)$ and $D(\Omega)$, are distinct. And they possess sufficient regularity such that

$$\omega_h \times \boldsymbol{u}_h \in \left[L^2(\Omega)\right]^2, \quad \forall \left(\omega_h, \boldsymbol{u}_h\right) \in C(\Omega) \times D(\Omega). \tag{10}$$

Trace spaces of finite dimensional spaces $C(\Omega,\Gamma)$ and $D(\Omega,\Gamma)$ on boundary section Γ are denoted by

$$\mathcal{T}C(\Omega,\Gamma) := \left\{ \mathcal{T}\omega_h \mid \omega_h \in C(\Omega) \right\},$$
$$\mathcal{T}D(\Omega,\Gamma) := \left\{ \mathcal{T}\boldsymbol{u}_h \mid \boldsymbol{u}_h \in D(\Omega) \right\}.$$

And we will also use following subspaces,

$$C_0(\Omega,\Gamma) := \left\{ \omega_h \,\middle|\, \omega_h \in C(\Omega),\ \mathcal{T}\omega_h = 0 \in \mathcal{T}C(\Omega,\Gamma) \right\},$$
$$D_0(\Omega,\Gamma) := \left\{ \boldsymbol{u}_h \,\middle|\, \boldsymbol{u}_h \in D(\Omega),\ \mathcal{T}\boldsymbol{u}_h = 0 \in \mathcal{T}D(\Omega,\Gamma) \right\}.$$

2.2. The formulation

We introduce a trilinear form

$$a\left(\rho_h, \vartheta_h, \boldsymbol{e}_h\right) := \int_\Omega \left(\rho_h \times \vartheta_h\right) \cdot \boldsymbol{e}_h \, \mathrm{d}\Omega,$$

for $\left(\rho_h, \vartheta_h, \boldsymbol{e}_h\right) \in C(\Omega) \times D(\Omega) \times D(\Omega)$. Because $\rho_h \times \vartheta_h$ is pointwise perpendicular to ϑ_h, we know that

$$a\left(\rho_h, \vartheta_h, \vartheta_h\right) = 0. \tag{11}$$

A spatially discrete weak mixed formulation of (1) is written as follows: Given $\boldsymbol{f} \in \left[L^2(\Omega)\right]^2$ and natural boundary conditions, $\widehat{P} \in H^{1/2}(\Omega, \Gamma_{\widehat{P}})$ and $\widehat{u}_\parallel \in \mathcal{T} H(\mathrm{rot}; \Omega, \Gamma_\parallel)$, seek $\left(\boldsymbol{u}_h, \omega_h, P_h\right) \in D(\Omega) \times C(\Omega) \times S(\Omega)$, such that, $\forall \left(\boldsymbol{v}_h,\ \xi_h,\ q_h\right) \in D_0(\Omega, \Gamma_\perp) \times C_0(\Omega, \Gamma_{\widehat{\omega}}) \times S(\Omega)$,

$$\langle \partial_t \boldsymbol{u}_h, \boldsymbol{v}_h \rangle_\Omega + a\left(\omega_h, \boldsymbol{u}_h, \boldsymbol{v}_h\right) + \mathrm{Re}^{-1} \langle \nabla \times \omega_h, \boldsymbol{v}_h \rangle_\Omega - \langle P_h, \nabla \cdot \boldsymbol{v}_h \rangle_\Omega = \langle \boldsymbol{f}, \boldsymbol{v}_h \rangle_\Omega - \left\langle \widehat{P}, \mathcal{T} \boldsymbol{v}_h \right\rangle_{\Gamma_{\widehat{P}}}, \tag{12a}$$

$$\langle \boldsymbol{u}_h, \nabla \times \xi_h \rangle_\Omega - \langle \omega_h, \xi_h \rangle_\Omega = \left\langle \widehat{u}_\parallel, \mathcal{T} \xi_h \right\rangle_{\Gamma_\parallel}, \tag{12b}$$

$$\langle \nabla \cdot \boldsymbol{u}_h, q_h \rangle_\Omega = 0, \tag{12c}$$

subject to essential boundary conditions, $\mathcal{T} \boldsymbol{u}_h = \widehat{u}_\perp \in \mathcal{T} D(\Omega, \Gamma_\perp)$ and $\mathcal{T} \omega_h = \widehat{\omega} \in \mathcal{T} C(\Omega, \Gamma_{\widehat{\omega}})$, and initial conditions $\left(\boldsymbol{u}_h^0, \omega_h^0\right) \in D(\Omega) \times C(\Omega)$.

One can show that solutions to the continuous version of (12) weakly solves the incompressible Navier-Stokes equations (1). A similar setup can be found in the work of Gawlik and Gay-Balmaz, see the fluid part of (48)–(53) in [16], where a mass, energy, cross-helicity and $\nabla \cdot \boldsymbol{B} = 0$ (divergence-free magnetic field) preserving formulation for incompressible magnetohydrodynamics (MHD) problems is introduced. And Hanot has used a three-dimensional counterpart of the present spatial discretization in [8].

3. Dissipation and conservation properties

In this section, we study dissipation and conservation properties of the formulation (12). The equivalence between (12) and the formulation used in the original MEEVC scheme, see (19) of [5], will also be shown. Thus, we will prove that the formulation (12) is also MEEVC. To this end, analyses conducted here are under conditions that (i) the domain is periodic ($\partial\Omega = \emptyset$) and (ii) there is no external force as in [5].

3.1. Mass conservation

Pointwise mass conservation is obviously satisfied; $\boldsymbol{u}_h$ is selected to be in $D(\Omega) \subset H(\mathrm{div}; \Omega)$ and the relation (12c) strongly enforces $\nabla \cdot \boldsymbol{u}_h = 0$ everywhere in Ω. This is a consequence of the fact that $\nabla\cdot$ maps $D(\Omega)$ into $S(\Omega)$, see (9).

3.2. Energy dissipation and conservation

For the energy balance, if we replace $\boldsymbol{v}_h$ in (12a) by $\boldsymbol{u}_h \in D(\Omega)$, we will obtain

$$\langle \partial_t \boldsymbol{u}_h, \boldsymbol{u}_h \rangle_\Omega + a\left(\omega_h, \boldsymbol{u}_h, \boldsymbol{u}_h\right) + \mathrm{Re}^{-1} \langle \nabla \times \omega_h, \boldsymbol{u}_h \rangle_\Omega - \langle P_h, \nabla \cdot \boldsymbol{u}_h \rangle_\Omega = 0. \tag{13}$$

The second and fourth terms vanish because of (11) and the pointwise mass conservation, i.e., $\nabla \cdot \boldsymbol{u}_h = 0$, respectively. This leads to

$$\langle \partial_t \boldsymbol{u}_h, \boldsymbol{u}_h \rangle_\Omega + \mathrm{Re}^{-1} \langle \nabla \times \omega_h, \boldsymbol{u}_h \rangle_\Omega = 0.$$

And from (12b), we know

$$\langle \boldsymbol{u}_h, \nabla \times \omega_h \rangle_\Omega = \langle \omega_h, \omega_h \rangle_\Omega,$$

because $\omega_h \in C(\Omega)$. Combining these two relations gives a (semi-)discrete energy balance,

$$\partial_t \mathcal{K}_h = \langle \partial_t \boldsymbol{u}_h, \boldsymbol{u}_h \rangle_\Omega = -\mathrm{Re}^{-1} \langle \omega_h, \omega_h \rangle_\Omega = -2\mathrm{Re}^{-1} \mathcal{E}_h, \tag{14}$$

where $\mathcal{K}_h = \frac{1}{2} \langle \boldsymbol{u}_h, \boldsymbol{u}_h \rangle_\Omega$ and $\mathcal{E}_h = \frac{1}{2} \langle \omega_h, \omega_h \rangle_\Omega$ are the discrete (total kinetic) energy and (total) enstrophy, respectively. It is consistent with (4), the energy balance of the strong form. Thus, (14) clearly implies discrete energy conservation in the inviscid limit ($\mathrm{Re} \to \infty$).

3.3. Enstrophy dissipation and conservation

If we take the time derivative of (12b), we obtain

$$\langle \partial_t \boldsymbol{u}_h, \nabla \times \xi_h \rangle_\Omega = \langle \partial_t \omega_h, \xi_h \rangle_\Omega , \quad \forall \xi_h \in C(\Omega) . \tag{15}$$

And, from (12a), we know that, $\forall\ \xi_h \in C(\Omega)$, (12a) must hold for $\nabla \times \xi_h \in D(\Omega)$, namely,

$$\langle \partial_t \boldsymbol{u}_h, \nabla \times \xi_h \rangle_\Omega + a\left(\omega_h, \boldsymbol{u}_h, \nabla \times \xi_h\right) + \mathrm{Re}^{-1} \langle \nabla \times \omega_h, \nabla \times \xi_h \rangle_\Omega - \langle P_h, \nabla \cdot \nabla \times \xi_h \rangle_\Omega = 0, \tag{16}$$

where the term $\langle P_h, \nabla \cdot \nabla \times \xi_h \rangle_\Omega$ vanishes because $\nabla \cdot \nabla \times (\cdot) \equiv 0$. If we further insert (15) into (16), we obtain

$$\langle \partial_t \omega_h, \xi_h \rangle_\Omega + a\left(\omega_h, \boldsymbol{u}_h, \nabla \times \xi_h\right) + \mathrm{Re}^{-1} \langle \nabla \times \omega_h, \nabla \times \xi_h \rangle_\Omega = 0, \quad \forall \xi_h \in C(\Omega) . \tag{17}$$

We can replace ξ_h in (17) by $\omega_h \in C(\Omega)$ and get

$$\langle \partial_t \omega_h, \omega_h \rangle_\Omega + a\left(\omega_h, \boldsymbol{u}_h, \nabla \times \omega_h\right) + \mathrm{Re}^{-1} \langle \nabla \times \omega_h, \nabla \times \omega_h \rangle_\Omega = 0 . \tag{18}$$

As $\boldsymbol{u}_h \in D(\Omega)$ and $\nabla \cdot \boldsymbol{u}_h = 0$ is satisfied pointwise, we can find a stream function $\psi_h \in C(\Omega)$ on a contractible domain such that $\boldsymbol{u}_h = \nabla \times \psi_h$. Recall the following vector calculus identity,

$$\omega_h \times \nabla \times \psi_h = \nabla \left(\omega_h \psi_h\right) - \psi_h \times \nabla \times \omega_h .$$

Thus, we know

$$\begin{aligned} a\left(\omega_h, \boldsymbol{u}_h, \nabla \times \omega_h\right) &= \int_\Omega \nabla \left(\omega_h \psi_h\right) \cdot \left(\nabla \times \omega_h\right) \mathrm{d}\Omega - a\left(\psi_h, \nabla \times \omega_h, \nabla \times \omega_h\right) \\ &= -\int_\Omega \omega_h \psi_h \left(\nabla \cdot \nabla \times \omega_h\right) \mathrm{d}\Omega - a\left(\psi_h, \nabla \times \omega_h, \nabla \times \omega_h\right), \end{aligned}$$

where we have performed integration by parts with respect to the gradient operator for the first term of the second equality and use the periodic boundary condition. Obviously, these terms vanish because of property $\nabla \cdot \nabla \times (\cdot) \equiv 0$ and (11). Therefore, we know that

$$a\left(\omega_h, \boldsymbol{u}_h, \nabla \times \omega_h\right) = 0, \tag{19}$$

and (18) leads to the following (semi-)discrete enstrophy balance,

$$\langle \partial_t \omega_h, \omega_h \rangle_\Omega = -\mathrm{Re}^{-1} \langle \nabla \times \omega_h, \nabla \times \omega_h \rangle_\Omega = -2\mathrm{Re}^{-1} \mathcal{P}_h , \tag{20}$$

where $\mathcal{P}_h := \frac{1}{2} \langle \nabla \times \omega_h, \nabla \times \omega_h \rangle_\Omega$ is the discrete (total) palinstrophy. (20) correctly reflects the enstrophy balance of the strong form, see (5). And, in the inviscid limit ($\mathrm{Re} \to \infty$), (20) leads to enstrophy conservation.

3.4. Vorticity conservation

For conservation of (total) vorticity, if we select $\xi_h = 1$ in (16), it is straightforward to find that

$$\partial_t \mathcal{W}_h = \langle \partial_t \omega_h, 1 \rangle_\Omega = 0,$$

which implies that vorticity is conserved over time. Moreover, by selecting $\xi_h = 1$ in (12b), we know that in periodic domains

$$\mathcal{W}_h \equiv 0,$$

which is consistent with (6) of the strong form.

3.5. Equivalence to the original MEEVC formulation

In addition to the regularity (10), suppose the finite dimensional spaces ensure

$$\omega_h \times \boldsymbol{u}_h \in H\left(\mathrm{rot}; \Omega\right) \subset \left[L^2(\Omega)\right]^2, \quad \forall \left(\omega_h, \boldsymbol{u}_h\right) \in C(\Omega) \times D(\Omega). \tag{21}$$

Then if we apply integration by parts to the second term of (17), we obtain

$$\langle \partial_t \omega_h, \xi_h \rangle_\Omega + \left\langle \nabla \times \left(\omega_h \times \boldsymbol{u}_h\right), \xi_h \right\rangle_\Omega + \mathrm{Re}^{-1} \langle \nabla \times \omega_h, \nabla \times \xi_h \rangle_\Omega = 0. \tag{22}$$

Recall that the identity, providing $\nabla \cdot \boldsymbol{u}_h = 0$,

$$\nabla \times \left(\omega_h \times \boldsymbol{u}_h\right) = \frac{1}{2} \left(\boldsymbol{u}_h \cdot \nabla\right) \omega_h + \frac{1}{2} \nabla \cdot \left(\omega_h \boldsymbol{u}_h\right), \tag{23}$$

is valid in two-dimensions. Using this identity, the following substitution can be employed in the weak form of the vorticity evolution equation (22),

$$\begin{aligned}\left\langle \nabla\times\left(\omega_h\times\boldsymbol{u}_h\right),\xi_h\right\rangle_\Omega &= \frac{1}{2}\left\langle\left(\boldsymbol{u}_h\cdot\nabla\right)\omega_h,\xi_h\right\rangle_\Omega+\frac{1}{2}\left\langle\nabla\cdot\left(\omega_h\boldsymbol{u}_h\right),\xi_h\right\rangle_\Omega\\ &= -\frac{1}{2}\left\langle\omega_h,\nabla\cdot\left(\xi_h\boldsymbol{u}_h\right)\right\rangle_\Omega+\frac{1}{2}\left\langle\nabla\cdot\left(\omega_h\boldsymbol{u}_h\right),\xi_h\right\rangle_\Omega,\end{aligned} \tag{24}$$

where the following integration by parts was used,

$$\left\langle\left(\boldsymbol{u}_h\cdot\nabla\right)\omega_h,\xi_h\right\rangle_\Omega=-\left\langle\omega_h,\nabla\cdot\left(\xi_h\boldsymbol{u}_h\right)\right\rangle_\Omega.$$

Thus, $\forall\xi_h\in C(\Omega)$, (22) can be written as

$$\langle\partial_t\omega_h,\xi_h\rangle_\Omega-\frac{1}{2}\left\langle\omega_h,\nabla\cdot\left(\xi_h\boldsymbol{u}_h\right)\right\rangle_\Omega+\frac{1}{2}\left\langle\nabla\cdot\left(\omega_h\boldsymbol{u}_h\right),\xi_h\right\rangle_\Omega+\mathrm{Re}^{-1}\langle\nabla\times\omega_h,\nabla\times\xi_h\rangle_\Omega=0, \tag{25}$$

which is the weak evolution equation for vorticity (as a replacement of (12b)) in the original MEEVC scheme, see (19) of [5]. If we select ξ_h to be ω_h in (25), the second and third terms cancel, we again get the same enstrophy balance, i.e., (20).

In the original MEEVC work, the reason behind using the identity (23) is to replace the weak nonlinear advection term by (24). By doing so, it is possible to construct another trilinear form for the nonlinear advection term in the weak vorticity evolution equation which is skew-symmetric with respect to entries ω_h and ξ_h, i.e.,

$$b(\omega_h,\boldsymbol{u}_h,\xi_h)=-b(\xi_h,\boldsymbol{u}_h,\omega_h),$$

see second and third terms in (25). This then implies that

$$b(\omega_h,\boldsymbol{u}_h,\omega_h)=0,$$

which, for the original MEEVC work, is a key requirement to obtain enstrophy conservation even when the numerical quadrature is inexact. However, this prevents the direct incorporation of boundary conditions for the tangential component of velocity because the port, i.e., the boundary integral term in (12b) which is used to impose them weakly, is missing. In this present work, we surprisingly find that, to setup a MEEVC scheme, we can bypass the construction of the skew-symmetric advection term as in the original MEEVC scheme and, thus, it is not necessary to introduce a second evolution equation for vorticity. This simplifies the formulation and also enables the direct application of no-slip boundary conditions.

4. Temporal discretization

For the temporal discretization, the classic implicit midpoint method [17] is used. The fully discrete version of (12) is written as: Given $\boldsymbol{f}\in\left[L^2(\Omega)\right]^2$ and natural boundary conditions, $\widehat{P}\in H^{1/2}(\Omega,\Gamma_{\widehat{P}})$ and $\widehat{u}_\parallel\in\mathcal{T}H(\mathrm{rot};\Omega,\Gamma_\parallel)$, for $k\in\{1,2,3,\cdots\}$, seek $\left(\boldsymbol{u}_h^k,\omega_h^k,P_h^{k-\frac{1}{2}}\right)\in D(\Omega)\times C(\Omega)\times S(\Omega)$, such that, $\forall\left(\boldsymbol{v}_h,\ \xi_h,\ q_h\right)\in D_0(\Omega,\Gamma_\perp)\times C_0(\Omega,\Gamma_{\widehat{\omega}})\times S(\Omega)$,

$$\begin{aligned}&\left\langle\frac{\boldsymbol{u}_h^k-\boldsymbol{u}_h^{k-1}}{\Delta t},\boldsymbol{v}_h\right\rangle_\Omega+a\left(\frac{\omega_h^{k-1}+\omega_h^k}{2},\frac{\boldsymbol{u}_h^{k-1}+\boldsymbol{u}_h^k}{2},\boldsymbol{v}_h\right)+\mathrm{Re}^{-1}\left\langle\nabla\times\frac{\omega_h^{k-1}+\omega_h^k}{2},\boldsymbol{v}_h\right\rangle_\Omega-\left\langle P_h^{k-\frac{1}{2}},\nabla\cdot\boldsymbol{v}_h\right\rangle_\Omega\\ &\quad=\left\langle\boldsymbol{f}^{k-\frac{1}{2}},\boldsymbol{v}_h\right\rangle_\Omega-\left\langle\widehat{P}^{k-\frac{1}{2}},\mathcal{T}\boldsymbol{v}_h\right\rangle_{\Gamma_{\widehat{P}}},\end{aligned} \tag{26a}$$

$$\left\langle\boldsymbol{u}_h^k,\nabla\times\xi_h\right\rangle_\Omega-\left\langle\omega_h^k,\xi_h\right\rangle_\Omega=\left\langle\widehat{u}_\parallel^k,\mathcal{T}\xi_h\right\rangle_{\Gamma_\parallel}, \tag{26b}$$

$$\left\langle\nabla\cdot\boldsymbol{u}_h^k,q_h\right\rangle_\Omega=0, \tag{26c}$$

where $\Delta t=t_k-t_{k-1}>0$, $\boldsymbol{u}_h^k=\boldsymbol{u}_h(\boldsymbol{x},t_k)$ (see (2)), subject to essential boundary conditions, $\mathcal{T}\boldsymbol{u}_h^k=\widehat{u}_\perp\in\mathcal{T}D(\Omega,\Gamma_\perp)$ and $\mathcal{T}\omega_h^k=\widehat{\omega}\in\mathcal{T}C(\Omega,\Gamma_{\widehat{\omega}})$, and initial conditions $\left(\boldsymbol{u}_h^0,\omega_h^0\right)\in D(\Omega)\times C(\Omega)$.

At the fully discrete level, if we repeat the analysis in Section 3 now for the fully discrete formulation (26), we can find that pointwise conservation of mass is satisfied at each time instant, see (26c), i.e.,

$$\nabla\cdot\boldsymbol{u}_h^k=0$$

everywhere in Ω. And we can also obtain dissipation rates,

$$\frac{\mathcal{K}_h^k-\mathcal{K}_h^{k-1}}{\Delta t}=\left\langle\frac{\boldsymbol{u}_h^k-\boldsymbol{u}_h^{k-1}}{\Delta t},\frac{\boldsymbol{u}_h^{k-1}+\boldsymbol{u}_h^k}{2}\right\rangle_\Omega=-\mathrm{Re}^{-1}\left\langle\omega_h^{k-\frac{1}{2}},\omega_h^{k-\frac{1}{2}}\right\rangle_\Omega=-2\mathrm{Re}^{-1}\mathcal{E}_h^{k-\frac{1}{2}}, \tag{27}$$

$$\frac{\mathcal{E}_h^k-\mathcal{E}_h^{k-1}}{\Delta t}=\left\langle\frac{\omega_h^k-\omega_h^{k-1}}{\Delta t},\frac{\omega_h^{k-1}+\omega_h^k}{2}\right\rangle_\Omega=-\mathrm{Re}^{-1}\left\langle\nabla\times\omega_h^{k-\frac{1}{2}},\nabla\times\omega_h^{k-\frac{1}{2}}\right\rangle_\Omega=-2\mathrm{Re}^{-1}\mathcal{P}_h^{k-\frac{1}{2}}, \tag{28}$$

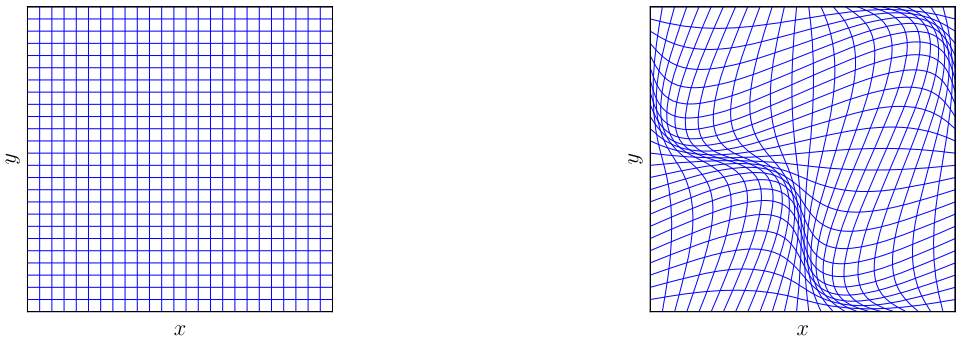

Fig. 1. Illustrations of meshes implied by (29) for $K = 25$, deformation factor $c = 0$ (left) and $c = 0.25$ (right).

and

$$\frac{\mathcal{W}_h^k - \mathcal{W}_h^{k-1}}{\Delta t} = \left\langle \frac{\omega_h^k - \omega_h^{k-1}}{\Delta t}, 1 \right\rangle_\Omega = 0,$$

where $\omega_h^{k-\frac{1}{2}} := \frac{\omega_h^{k-1} + \omega_h^k}{2}$. This shows that at the fully discrete level the proposed scheme is also MEEVC in the inviscid limit, $\mathrm{Re} \to \infty$.

5. Numerical tests

Five tests are conducted in this work. The accuracy of the method is investigated with an analytical solution in Section 5.1. Conservation and dissipation properties are tested in Section 5.2. The original MEEVC scheme experiences difficulties of handling no-slip boundary conditions [6] while imposing different boundary conditions including the no-slip ones is straightforward for the method studied in this work. This is demonstrated in Section 5.1, Section 5.3 and Section 5.4. Numerical evidences of (19) are given by the test in Section 5.5.

We use the mimetic polynomial spaces, which satisfy the discrete de Rham complex (9), the regularity (10) and the regularity (21), as the finite dimensional spaces under the framework of the mimetic spectral element method, see, for example, [18] or [19, Chapter 2]. The degree of the polynomial spaces is denoted by N. The Newton-Raphson method is employed for solving the nonlinear systems. Note that any set of finite elements that forms the discrete de Rham complex (9) and satisfies the regularity (10) works. For example, in a triangulated conforming grid, Lagrange elements of degree N, Raviart–Thomas elements of degree N and discontinuous Lagrange elements of degree $(N-1)$ are a classic option. They are also the function spaces used in the original MEEVC scheme, see (13)-(18) of [5].

Both orthogonal and curvilinear meshes will be used in this work. Suppose a reference domain is $\mathring{\Omega} := (r, s) \in [0, 1]^2$. A uniform orthogonal mesh of $K \times K$ square elements is generated in the reference domain. This mesh is then distorted with a mapping, $\Phi : (r, s) \to (x, y)$, expressed as

$$\begin{cases} x = \alpha \left(r + \frac{1}{2} c \sin(2\pi r) \sin(2\pi s) \right) \\ y = \alpha \left(s + \frac{1}{2} c \sin(2\pi r) \sin(2\pi s) \right) \end{cases}, \tag{29}$$

where $\alpha > 0$ and $0 \le c \le 0.3$. It gives a mesh in $\Omega = (x, y) \in [0, \alpha]^2$, and the factor c is a deformation factor. When $c = 0$ the mesh is orthogonal and uniform, and when $c > 0$ the mesh is curvilinear. See Fig. 1 for illustrations of this mesh. And see [20] for an introduction on mesh deformation.

Implementations of the present work are done in *Python*.

5.1. Accuracy test: Taylor–Green vortex

We test the accuracy of the method using a classic analytical solution of two-dimensional incompressible Navier-Stokes equations in the absence of external force, the Taylor–Green vortex, written as

$$\begin{aligned} u(x, y, t) &= -\sin(\pi x) \cos(\pi y) e^{-2\pi^2 t/\mathrm{Re}}, \\ v(x, y, t) &= \cos(\pi x) \sin(\pi y) e^{-2\pi^2 t/\mathrm{Re}}, \\ p(x, y, t) &= \frac{1}{4} \left(\cos(2\pi x) + \cos(2\pi y) \right) e^{-4\pi^2 t/\mathrm{Re}}, \\ \omega(x, y, t) &= -2\pi \sin(\pi x) \sin(\pi y) e^{-2\pi^2 t/\mathrm{Re}}. \end{aligned}$$

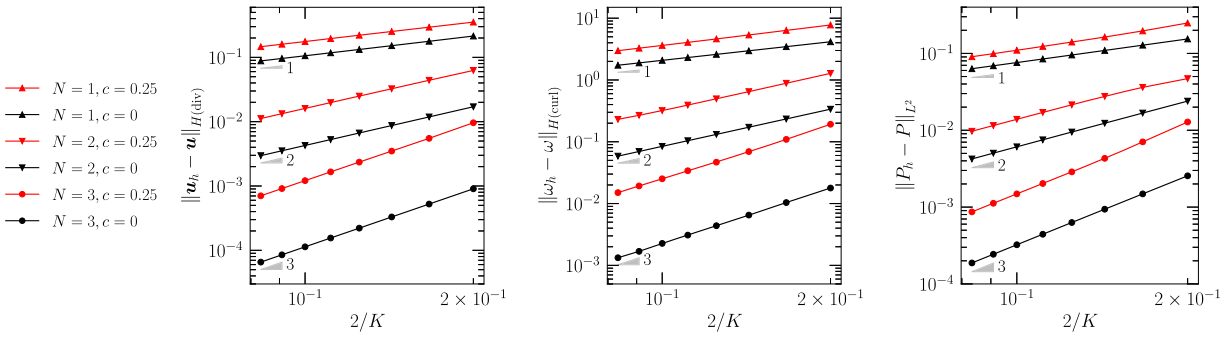

Fig. 2. $H(\mathrm{div})$-error of $\boldsymbol{u}_h$, $H(\mathrm{curl})$-error of ω_h and L^2-error of P_h at $t = 1$ of the Taylor–Green vortex test with periodic boundary conditions under *ph*-refinements for $N \in \{1,2,3\}$, $c \in \{0, 0.25\}$, $K \in \{10, 12, 14 \cdots, 24\}$, $\Delta t = \frac{1}{25}$ and $\mathrm{Re} = 100$.

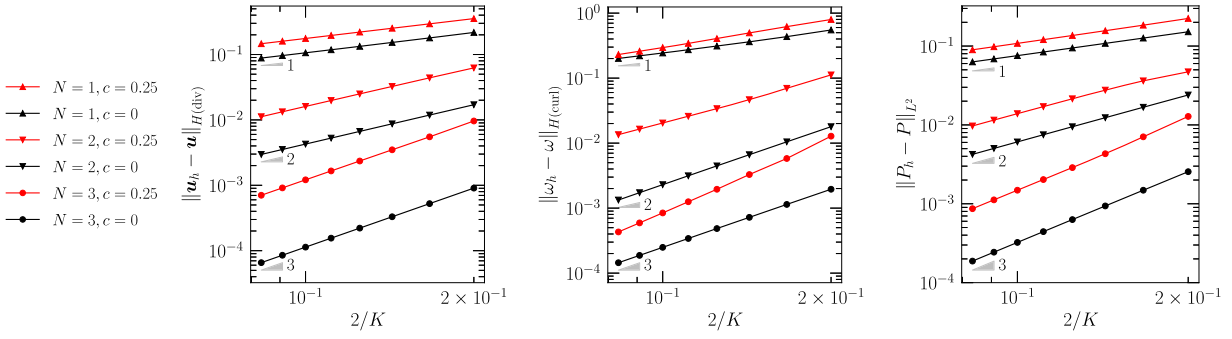

Fig. 3. $H(\mathrm{div})$-error of $\boldsymbol{u}_h$, $H(\mathrm{curl})$-error of ω_h and L^2-error of P_h at $t = 1$ of the Taylor–Green vortex test with no-slip boundary conditions under *ph*-refinements for $N \in \{1,2,3\}$, $c \in \{0, 0.25\}$, $K \in \{10, 12, 14, \cdots, 24\}$, $\Delta t = \frac{1}{25}$ and $\mathrm{Re} = 100$.

The domain is set to $\Omega = (x, y) \in [0, 2]^2$. We use the meshes described by (29) of $c \in \{0, 0.25\}$ and solve the Taylor–Green vortex from $t = t_0 = 0$ to $t = 1$ under *ph*-refinements for $N \in \{1, 2, 3\}$ and $K \in \{10, 12, 14, \cdots, 24\}$ with $\mathrm{Re} = 100$ and $\Delta t = \frac{1}{25}$. Two sets of tests are conducted. The first set is with periodic boundary conditions and the second one is with following no-slip boundary conditions,

$$\Gamma_{\hat{P}} := \Gamma_{\mathrm{left}} \cup \Gamma_{\mathrm{bottom}}, \ \Gamma_{\parallel} = \partial\Omega,$$

where Γ_{left} and Γ_{bottom} are the left and bottom faces of the square domain. Results are presented in Fig. 2 and Fig. 3. Optimal convergence rates are observed in both sets of results.

5.2. Conservation and dissipation tests: Shear layer roll-up

The shear layer roll-up is a two-dimensional ideal flow whose components of the initial condition, $\boldsymbol{u}^0 = \begin{bmatrix} u^0 & v^0 \end{bmatrix}^{\mathsf{T}}$, are given by

$$u^0 = \begin{cases} \tanh\left(\dfrac{y - \pi/2}{\delta}\right), & y \leq \pi \\ \tanh\left(\dfrac{3\pi/2 - y}{\delta}\right), & y > \pi \end{cases}, \qquad v^0 = \epsilon \sin(x),$$

where $\delta = \frac{\pi}{15}$ and $\epsilon = 0.05$, see [5,21]. The domain is $\Omega = (x, y) \in [0, 2\pi]^2$ with periodic boundary conditions. Meshes as described in (29) for $c \in \{0, 0.25\}$ and $K = 48$ are used. The polynomial degree is set to $N = 2$ and the time interval is $\Delta t = \frac{1}{50}$. The flow is computed from $t = t_0 = 0$ to $t = 8$. To limit the error caused by the Newton-Raphson method, the tolerance of outer iterations is set to 10^{-12}. The vorticity field ω_h at $t \in \{0, 4, 8\}$ for $c = 0$ is shown in Fig. 4. In Fig. 5, results showing the conservation laws are satisfied to machine precision on both orthogonal and curvilinear meshes are presented. And throughout this section we use $\|\nabla \cdot \boldsymbol{u}_h\|_{L^2}$, i.e. the L^2-norm of $\nabla \cdot \boldsymbol{u}_h$, to identify mass conservation. Since the basis functions have normal continuity, if $\|\nabla \cdot \boldsymbol{u}_h\|_{L^2} = 0$ (to machine precision), pointwise mass conservation is satisfied everywhere.

We repeat the above test now for a viscous flow of $\mathrm{Re} = 500$. The results are presented in Fig. 6. It is seen that, to machine precision, (i) mass and vorticity conservation and (ii) energy and enstrophy balances, (27) and (28), are satisfied for both orthogonal and curvilinear meshes.

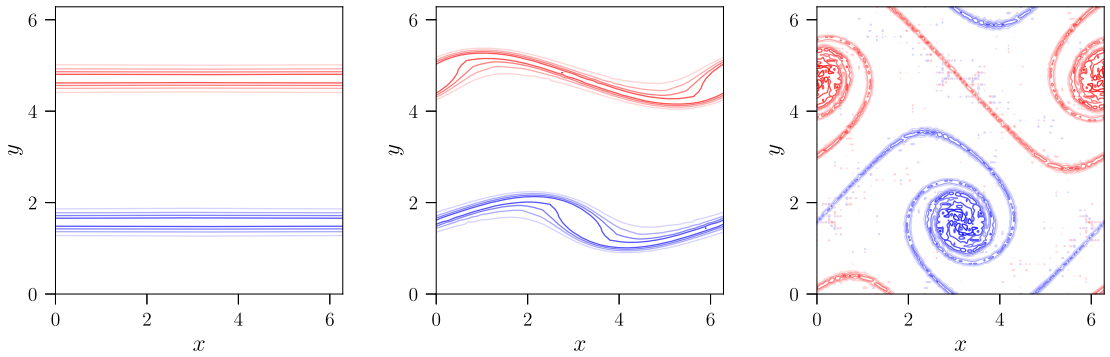

Fig. 4. Vorticity field ω_h of the ideal shear layer roll-up test at $t \in \{0, 4, 8\}$ with contour lines for $\omega_h \in \{\pm 1, \pm 2, \pm 3, \cdots, \pm 6\}$. The color scheme is from blue ($-6 \leftarrow \omega_h$) to red ($\omega_h \rightarrow 6$). The simulation is conducted for $N = 2$, $c = 0$, $K = 48$, $\Delta t = \frac{1}{50}$. (For interpretation of the colors in the figure(s), the reader is referred to the web version of this article.)

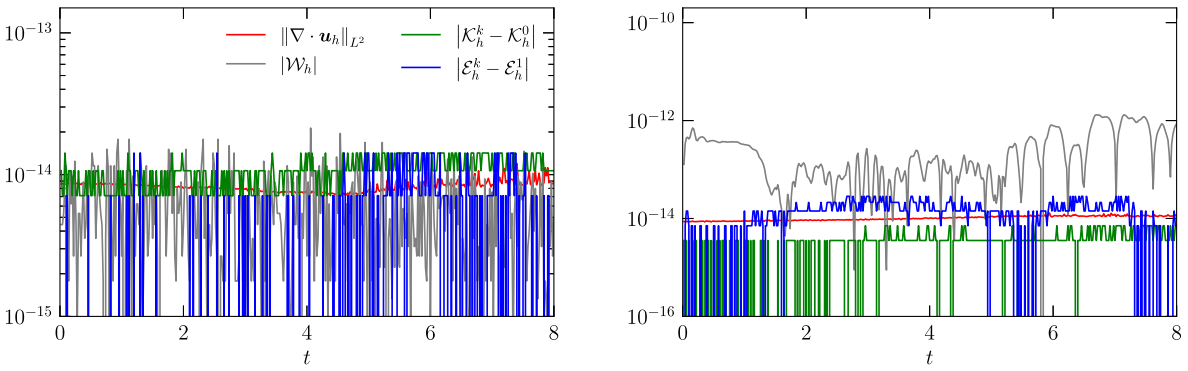

Fig. 5. Discrete mass, energy, enstrophy and vorticity conservation over time of the ideal shear layer roll-up test for $N = 2$, $c = 0$ (left), $c = 0.25$ (right), $K = 48$ and $\Delta t = \frac{1}{50}$.

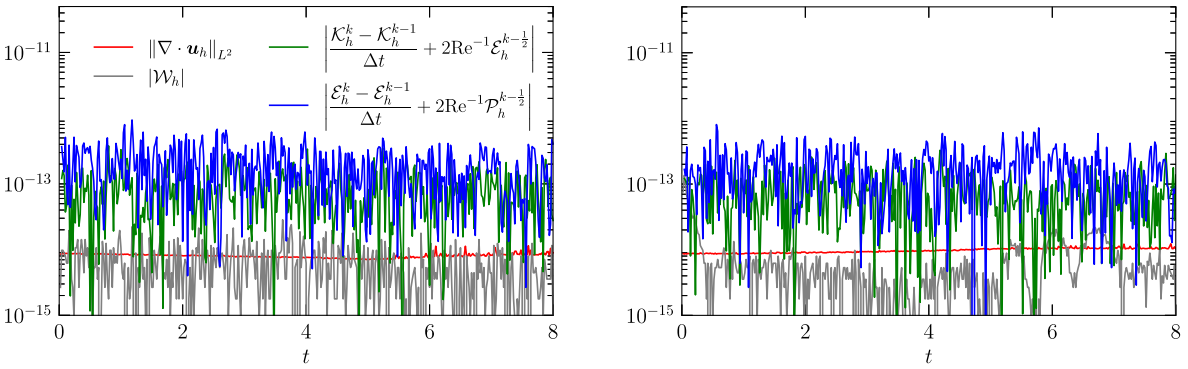

Fig. 6. Discrete mass conservation, energy and enstrophy balances, and vorticity conservation over time of the viscous shear layer roll-up test for $N = 2$, $c = 0$ (left), $c = 0.25$ (right), $K = 48$, $\Delta t = \frac{1}{50}$ and $\mathrm{Re} = 500$.

5.3. General boundary condition test 1: Normal dipole collision

The normal dipole collision is a viscous flow in the domain $\Omega = (x, y) \in [-1, 1]^2$ with no-slip boundary conditions on all four walls [22]. The unscaled initial velocity field, $\boldsymbol{u}^0 = \begin{bmatrix} u^0 & v^0 \end{bmatrix}^\mathsf{T}$, is given by

$$u^0 = -\frac{1}{2}\left|\omega_e\right|\left(y - y_1\right)e^{-(r_1/r_0)^2} + \frac{1}{2}\left|\omega_e\right|\left(y - y_2\right)e^{-(r_2/r_0)^2},$$
$$v^0 = -\frac{1}{2}\left|\omega_e\right|\left(x - x_2\right)e^{-(r_2/r_0)^2} + \frac{1}{2}\left|\omega_e\right|\left(x - x_1\right)e^{-(r_1/r_0)^2},$$

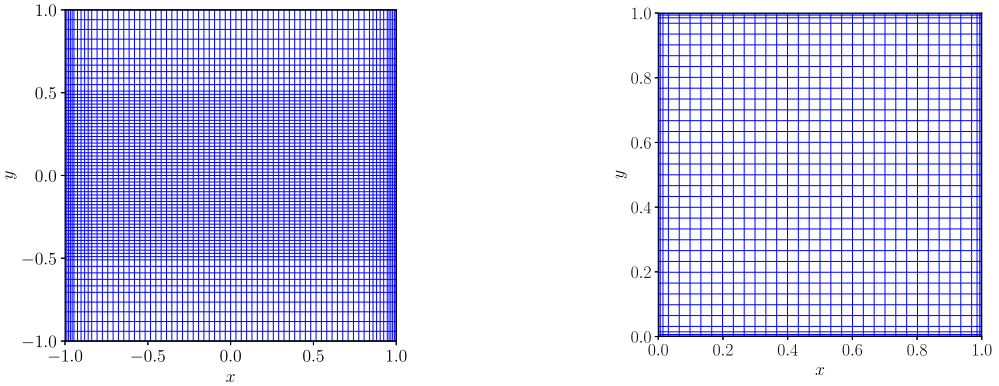

Fig. 7. Left: The mesh of 5148 elements used in the normal dipole collision test. Right: The mesh of 1296 elements used in the lid-driven cavity test.

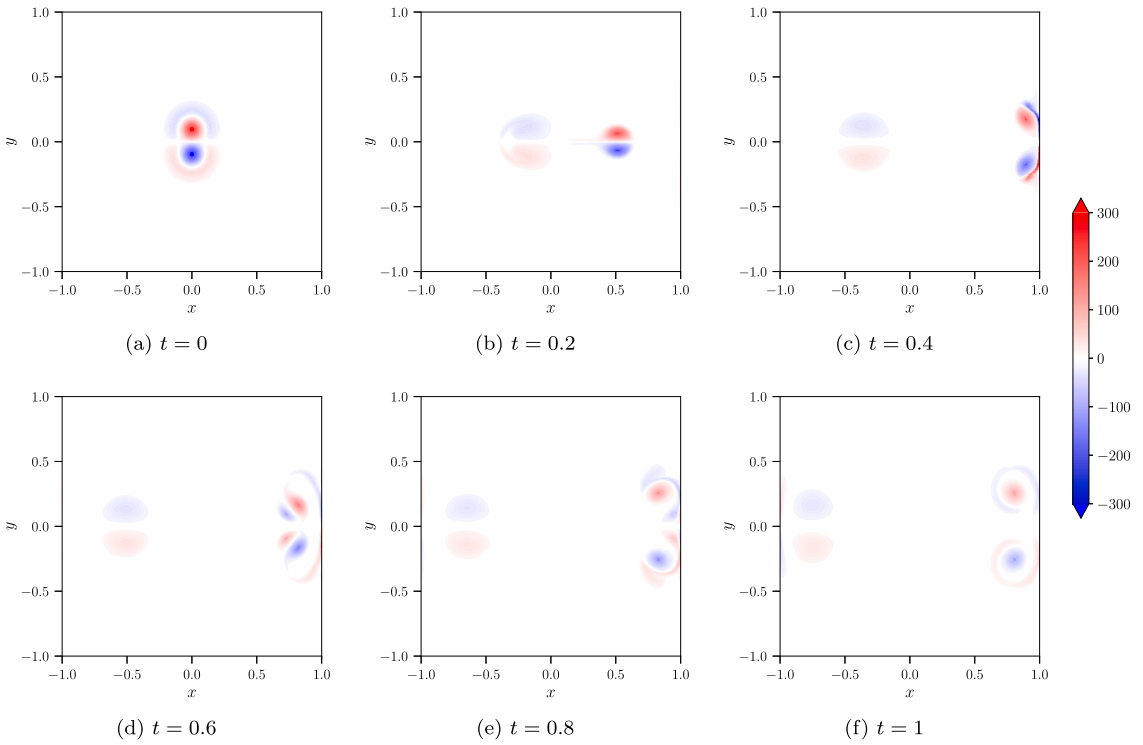

Fig. 8. Vorticity field ω_h at $t \in \left\{0, \frac{1}{5}, \frac{2}{5}, \cdots, 1\right\}$ of the normal dipole collision test in a mesh of 5148 elements for $N = 2$, $\Delta t = \frac{1}{200}$ and $\mathrm{Re} = 625$.

where $|\omega_e| = 320$, $(x_1, y_1) = (0, 0.1)$ and $(x_2, y_2) = (0, -0.1)$, r_1 and r_2 are distances to (x_1, y_1) and (x_2, y_2), respectively, and $r_0 = 0.1$. This velocity field leads to a vorticity field expressed as

$$\omega^0 = \sum_{i \in \{1,2\}} \omega_{e,i} \left(1 - \left(\frac{r_i}{r_0}\right)^2\right) e^{-(r_i/r_0)^2},$$

where $\omega_{e,1} = 320$, $\omega_{e,2} = -320$, which is a combination of two monopoles centered at (x_1, y_1) and (x_2, y_2), respectively. The initial velocity is then scaled such that the initial kinetic energy is $\mathcal{E}^0 = 2$. The scaling factor is $f \approx 0.936026$. The corresponding initial enstrophy and palinstrophy are $\mathcal{E}^0 \approx 800$ and $\mathcal{P}^0 \approx 441855$, respectively. The flow is absent of external body force. For the present test, we use a non-uniform orthogonal mesh of 5148 elements, see the left mesh in Fig. 7, $\mathrm{Re} = 625$, polynomial degree $N = 2$ and $\Delta t = \frac{1}{200}$. This setup is similar to that in [6] except that [6] uses an unstructured mesh and much smaller time steps, $\Delta t = \frac{1}{2000}$.

The dipole is initialized at $t = t_0 = 0$. It will move under a self-induced velocity in x^+-direction with an induced wake moving in the opposite direction. The simulation is performed until $t = 1$. The vorticity field ω_h at $t \in \left\{0, \frac{1}{5}, \frac{2}{5}, \cdots, 1\right\}$ is presented in Fig. 8.

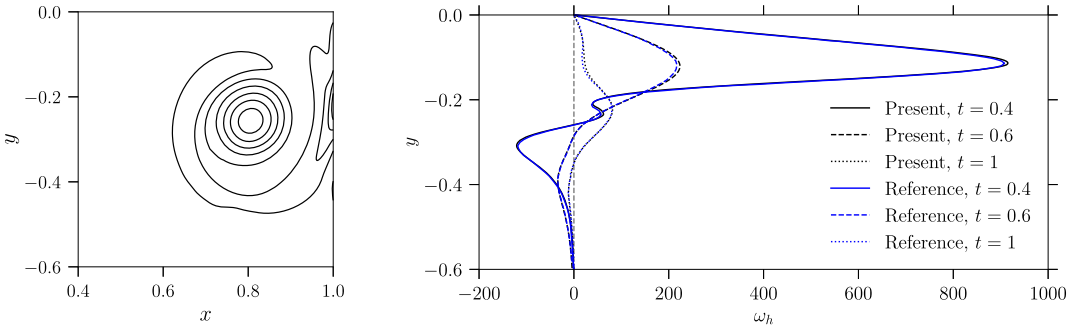

Fig. 9. Vorticity field ω_h in region $(x, y) \in [0.4, 1] \times [-0.6, 0]$ at $t = 1$ with contour lines for $\omega_h \in \{-90, -70, -50, \cdots, 70\}$ and on the boundary section $(x, y) \in -1 \times [-0.6, 0]$ at $t \in \{0.4, 0.6, 1\}$ compared to reference results taken from [22, Fig. 5] for $\mathrm{Re} = 625$. The present simulation has 145^2 degrees of freedom for vorticity. The reference simulation uses a pseudospectral method and has 256^2 degrees of freedom for vorticity.

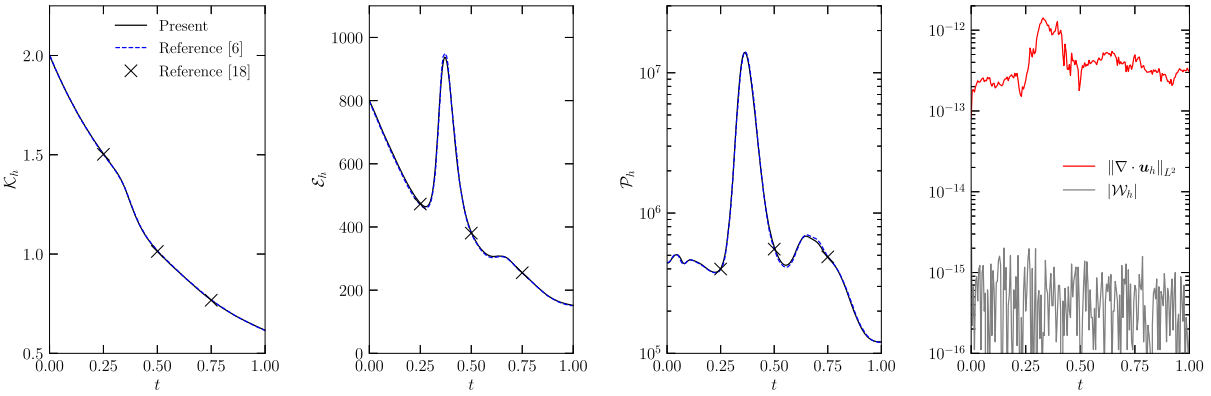

Fig. 10. Discrete energy, enstrophy, palinstrophy over time compared to reference results taken from [6, Fig. 8] and reference results at $t \in \{0.25, 0.5, 0.75\}$ taken from [22], and mass and vorticity conservation over time.

The original MEEVC scheme uses indirect approaches to impose no-slip boundary conditions, and the suggested approach, called the kinematic Neumann approach, destroys vorticity conservation, see [6, Fig. 9]. In contrast, the present method can handle no-slip boundary conditions (and other general boundary conditions) naturally, see the formulation (12) or (26). In Fig. 9, local distributions of vorticity field in region $(x, y) \in [0.4, 1] \times [-0.6, 0]$ at $t = 1$ and on boundary section $(x, y) \in -1 \times [-0.6, 0]$ at different time instants (with comparisons to results in [22]) are shown. The discrete energy, enstrophy and palinstrophy over time are presented and compared to results taken from [6,22] in Fig. 10 where mass and vorticity conservation is also shown. These results show an improved match with the reference than those in [6, Fig. 10] and also indicate that no-slip boundary conditions are correctly incorporated by the present method without destroying vorticity conservation.

5.4. General boundary condition test 2: Lid-driven cavity

In this section, we test the proposed method with the lid-driven cavity flow which is a classic benchmark of no-slip boundary conditions and singularities. The computational domain is a unit square, $\Omega = (x, y) \in [0, 1]^2$, and has four infinite no-slip walls. The flow is at rest initially. And from $t = t_0 = 0$, the top wall ($y = 1$), namely, the lid, moves left with a constant speed -1, i.e. $\boldsymbol{u}_{\text{lid}} = \begin{bmatrix} -1 & 0 \end{bmatrix}^{\mathsf{T}}$, and drives the viscous flow. Singularities appear at two top corners where vorticity and pressure approach infinity. The external body force is set to zero.

We do this test for $\mathrm{Re} = 1000$. A mesh of 1296 elements that are locally refined near the walls is used, see the right mesh in Fig. 7. Other parameters are the polynomial degree $N = 3$ and the time interval $\Delta t = \frac{1}{100}$. The simulation terminates when the flow reaches the steady state whose criterion is

$$\left\| \boldsymbol{u}_h^k - \boldsymbol{u}_h^{k-1} \right\|_{L^2} \leq 10^{-7}.$$

Results with comparisons to reference results from [23] are shown in Fig. 11 where we can see that the present method produces results matching the reference results well.

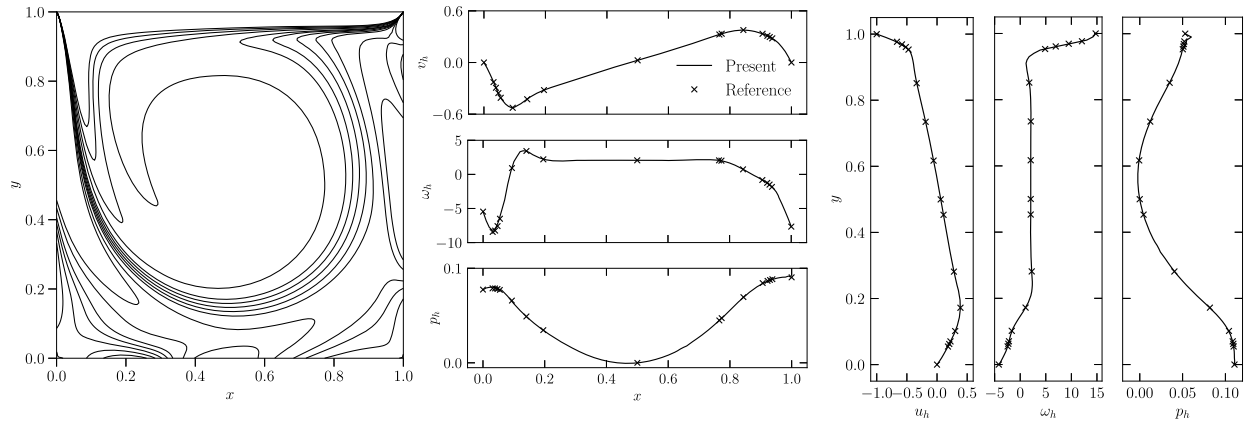

Fig. 11. Vorticity field ω_h (left, contour lines for $\omega_h \in \{-3,-2,-1,-0.5,0,0.5,1,2,3,4,5\}$), solutions v_h, ω_h and p_h along the horizontal centerline (middle) and solutions u_h, ω_h and p_h along the vertical centerline (right) at the steady state of the lid-driven cavity flow for $\mathrm{Re} = 1000$ with comparisons to reference results from [23, Table 9, Table 10]. u_h and v_h are two components of velocity, i.e. $\boldsymbol{u}_h = [u_h \quad v_h]^\mathsf{T}$. The reference results use polynomials of extremely high degrees, 160 and 158, for the approximation of velocity and pressure, respectively.

Table 1
$a\left(\omega_h, \boldsymbol{u}_h, \nabla\times\omega_h\right)$ for $c \in \{0, 0.25\}$, $K = 12$, $N \in \{2,3,4\}$ and $N_Q \in \{1,2,3,4,5,6\}$.

N_Q	c	0			0.25		
	N	2	3	4	2	3	4
1		$1.05e-12$	$4.72e-12$	$-7.59e-11$	$-1.91e+02$	$-6.93e+00$	$1.25e+01$
2		$-1.60e-12$	$2.25e-12$	$1.04e-12$	$-5.19e-12$	$7.43e+00$	$3.22e-01$
3		$2.81e-13$	$-1.01e-12$	$3.65e-14$	$6.51e-12$	$1.55e-03$	$-7.90e-02$
4		$1.65e-12$	$7.96e-13$	$1.01e-13$	$-7.46e-14$	$-9.95e-14$	$-1.48e-04$
5		$-5.22e-12$	$1.86e-12$	$-7.21e-14$	$1.70e-12$	$5.68e-13$	$-1.42e-13$
6		$3.46e-14$	$5.59e-15$	$1.71e-13$	$1.19e-13$	$-2.52e-13$	$2.23e-13$

5.5. Convective term for enstrophy conservation

This subsection provides numerical evidences for (19) as it is a key for the enstrophy balance of the present method. Given two random smooth scalar fields,

$$\omega = 2\pi \sin(2\pi x + e)\sin(2\pi y + f)$$

and

$$\psi = 2\pi \sin(2\pi x + g)\sin(2\pi y + h),$$

where $e, f, g, h \in (0,1)$ are random real numbers, in the periodic unit square, $\Omega = (x,y) \in [0,1]^2$. Meshes as described in (29) for $c \in \{0, 0.25\}$ and $K = 12$ are used. ω and ψ are projected to finite dimensional polynomial spaces as ω_h and ψ_h, see [18] or [19] for details of these projections. The finite dimensional velocity is $\boldsymbol{u}_h = \nabla\times\psi_h$ and thus $\nabla\cdot\boldsymbol{u}_h = 0$. Then the trilinear form $a\left(\omega_h, \boldsymbol{u}_h, \nabla\times\omega_h\right)$ is computed with Gauss quadrature, see [24], of different degrees, N_Q.

The results are presented in Table 1. We can see that, for the orthogonal mesh ($c = 0$), the trilinear form is zero (to machine precision) even when the quadrature is very inexact, for example, $N = 4$ and $N_Q = 1$ (numerical quadrature of degree N_Q is exact for polynomials of degree lower than or equal to $2N_Q - 1$). While for the curvilinear mesh ($c = 0.25$), as the metric of the mapping, see (29), cannot be captured by polynomials, the quadrature is always inexact and the trilinear form is still zero for quadrature degree that is significantly high. These results support the statement that, for $\nabla\cdot\boldsymbol{u}_h = 0$, the trilinear form $a\left(\omega_h, \boldsymbol{u}_h, \nabla\times\omega_h\right)$ can be zero even with inexact numerical quadrature.

6. Conclusions

In this work, we present a mass, energy, enstrophy and vorticity conserving (MEEVC) mixed finite element discretization for the rotational form of the incompressible Navier-Stokes equations on both orthogonal and curvilinear meshes. Comparing to the original MEEVC method, the present method uses a formulation of a single evolution equation and, more importantly, can naturally adapt no-slip boundary conditions without violating vorticity conservation. However, it does not linearize the discrete systems as the original MEEVC scheme does; a more expensive nonlinear method has to be employed to solve the systems.

CRediT authorship contribution statement

Yi Zhang: Writing – review & editing, Writing – original draft, Visualization, Validation, Software, Project administration, Methodology, Conceptualization. **Artur Palha:** Writing – review & editing, Writing – original draft, Methodology, Formal analysis. **Marc Gerritsma:** Writing – review & editing, Writing – original draft, Methodology, Formal analysis. **Qinghe Yao:** Writing – original draft, Methodology.

Declaration of competing interest

The authors declare that they have no known competing financial interests or personal relationships that could have appeared to influence the work reported in this paper.

Data availability

Data will be made available on request.

Acknowledgements

The authors acknowledge dr. Andrea Brugnoli for helpful discussions. We also want to thank the reviewers for their insightful comments.

Appendix A

In this appendix, we analyze mass and vorticity conservation, and balance of energy and enstrophy for the presented formulation under general boundary conditions, (12), as a complement to Section 3. Without the loss of generality, we use $\widehat{u}_\perp = 0$ and $\Gamma_\parallel = \partial\Omega$ (i.e. $\Gamma_{\widehat{\omega}} = \emptyset$ as $\Gamma_{\widehat{\omega}} \cup \Gamma_\parallel = \partial\Omega$ and $\Gamma_{\widehat{\omega}} \cap \Gamma_\parallel = \emptyset$).

Mass conservation Pointwise mass conservation, see Section 3.1, is always satisfied regardless of the boundary conditions.

Energy balance For the energy balance, if we replace $\boldsymbol{v}_h$ in (12a) by $\boldsymbol{u}_h \in D_0(\Omega, \Gamma_\perp)$, we will obtain

$$\langle \partial_t \boldsymbol{u}_h, \boldsymbol{u}_h \rangle_\Omega + a\left(\omega_h, \boldsymbol{u}_h, \boldsymbol{u}_h\right) + \mathrm{Re}^{-1} \langle \nabla \times \omega_h, \boldsymbol{u}_h \rangle_\Omega - \langle P_h, \nabla \cdot \boldsymbol{u}_h \rangle_\Omega = \langle \boldsymbol{f}, \boldsymbol{u}_h \rangle_\Omega - \left\langle \widehat{P}, \boldsymbol{\mathcal{T}} \boldsymbol{u}_h \right\rangle_{\Gamma_{\widehat{P}}},$$

which leads to

$$\langle \partial_t \boldsymbol{u}_h, \boldsymbol{u}_h \rangle_\Omega + \mathrm{Re}^{-1} \langle \nabla \times \omega_h, \boldsymbol{u}_h \rangle_\Omega = \langle \boldsymbol{f}, \boldsymbol{u}_h \rangle_\Omega - \left\langle \widehat{P}, \boldsymbol{\mathcal{T}} \boldsymbol{u}_h \right\rangle_{\Gamma_{\widehat{P}}},$$

for the same reasons as in Section 3.2. And from (12b), since $C(\Omega) = C_0(\Omega, \Gamma_{\widehat{\omega}})$ when $\Gamma_{\widehat{\omega}} = \emptyset$, we know

$$\langle \boldsymbol{u}_h, \nabla \times \omega_h \rangle_\Omega = \langle \omega_h, \omega_h \rangle_\Omega + \left\langle \widehat{u}_\parallel, \boldsymbol{\mathcal{T}} \boldsymbol{\omega}_h \right\rangle_{\Gamma_\parallel},$$

for $\omega_h \in C(\Omega)$. Combining these two relations gives a (semi-)discrete energy balance,

$$\partial_t \mathcal{K}_h = \underbrace{-2\mathrm{Re}^{-1} \mathcal{E}_h}_{\text{(i) dissipation}} \underbrace{+ \langle \boldsymbol{f}, \boldsymbol{u}_h \rangle_\Omega}_{\text{(ii) work body force}} \underbrace{- \left\langle \widehat{P}, \boldsymbol{\mathcal{T}} \boldsymbol{u}_h \right\rangle_{\Gamma_{\widehat{P}}}}_{\text{(iii) work normal force}} \underbrace{- \mathrm{Re}^{-1} \left\langle \widehat{u}_\parallel, \boldsymbol{\mathcal{T}} \boldsymbol{\omega}_h \right\rangle_{\Gamma_\parallel}}_{\text{(iv) work shear force}}. \tag{A.1}$$

This equation states that the time rate of change of kinetic energy is equal to the summation of (i) the amount of energy dissipation within the domain Ω per unit time and the amount of work done on the fluid per unit time. And the work is separated into (ii) the work done by the body force within the domain, (iii) the work done by the prescribed pressure along $\Gamma_{\widehat{P}}$, and (iv) the work done by the shear stress along $\Gamma_\parallel$, respectively.

In the special case where periodic boundary conditions are employed and the body force is set to zero, the energy balance, (14), is retrieved.

Enstrophy balance If we take the time derivative of (12b), we obtain

$$\langle \partial_t \boldsymbol{u}_h, \nabla \times \xi_h \rangle_\Omega = \langle \partial_t \omega_h, \xi_h \rangle_\Omega + \left\langle \partial_t \widehat{u}_\parallel, \boldsymbol{\mathcal{T}} \xi_h \right\rangle_{\Gamma_\parallel}, \quad \forall \xi_h \in C_0(\Omega, \Gamma_{\widehat{\omega}}).$$

However, since $\xi_h \in C_0(\Omega, \Gamma_{\widehat{\omega}})$ does not guarantee that $\nabla \times \xi_h \in D_0(\Omega, \Gamma_\perp)$, a replacement similar to the one used for (16) is no longer valid. Furthermore, inconsistency will arise again when we perform a replacement similar to the one used to derive (18). As a consequence, an enstrophy balance like the energy balance, i.e. (A.1), cannot be found by the authors for the current formulation. Although the results have supported it on handling general boundary conditions, this lack is an obvious limit of this work.

Vorticity conservation For vorticity conservation, we can derive, when $\widehat{u}_{\parallel} = 0$, from (12b) that

$$\mathcal{W}_h \equiv 0$$

by selecting

$$\xi_h = 1.$$

This is inline with the results shown in the right diagram of Fig. 10.

References

[1] T.A. Zang, On the rotation and skew-symmetric forms for incompressible flow simulations, Appl. Numer. Math. 7 (1) (1991) 27–40.
[2] W. Layton, C.C. Manica, M. Neda, M. Olshanskii, L.G. Rebholz, On the accuracy of the rotation form in simulations of the Navier–Stokes equations, J. Comput. Phys. 228 (9) (2009) 3433–3447.
[3] X. Zhang, D. Schmidt, B. Perot, Accuracy and conservation properties of a three-dimensional unstructured staggered mesh scheme for fluid dynamics, J. Comput. Phys. 175 (2) (2002) 764–791.
[4] J. Kreeft, M. Gerritsma, Mixed mimetic spectral element method for Stokes flow: a pointwise divergence-free solution, J. Comput. Phys. 240 (2013) 284–309.
[5] A. Palha, M. Gerritsma, A mass, energy, enstrophy and vorticity conserving (MEEVC) mimetic spectral element discretization for the 2D incompressible Navier-Stokes equations, J. Comput. Phys. 328 (2017) 200–220.
[6] G. de Diego, A. Palha, M. Gerritsma, Inclusion of no-slip boundary conditions in the MEEVC scheme, J. Comput. Phys. 378 (2019) 615–633.
[7] M. Olshanskii, L.G. Rebholz, Note on helicity balance of the Galerkin method for the 3D Navier–Stokes equations, Comput. Methods Appl. Mech. Eng. 199 (17–20) (2010) 1032–1035.
[8] M.-L. Hanot, An arbitrary order and pointwise divergence-free finite element scheme for the incompressible 3D Navier–Stokes equations, SIAM J. Numer. Anal. 61 (2) (2023) 784–811.
[9] P.W. Schroeder, C. Lehrenfeld, A. Linke, G. Lube, Towards computable flows and robust estimates for inf-sup stable FEM applied to the time-dependent incompressible Navier–Stokes equations, SeMA J. 75 (2018) 629–653.
[10] J.A. Evans, T.J. Hughes, Isogeometric divergence-conforming B-splines for the steady Navier–Stokes equations, Math. Models Methods Appl. Sci. 23 (08) (2013) 1421–1478.
[11] E.S. Gawlik, F. Gay-Balmaz, A conservative finite element method for the incompressible Euler equations with variable density, J. Comput. Phys. 412 (2020) 109439.
[12] D. Boffi, F. Brezzi, M. Fortin, et al., Mixed Finite Element Methods and Applications, vol. 44, Springer, 2013.
[13] P.B. Bochev, J.M. Hyman, Principles of mimetic discretizations of differential operators, in: Compatible Spatial Discretizations, Springer, New York, 2006, pp. 89–119.
[14] S.H. Christiansen, J. Hu, K. Hu, Nodal finite element de Rham complexes, Numer. Math. 139 (2) (2018) 411–446.
[15] J.T. Oden, L.F. Demkowicz, Applied Functional Analysis, second edition, Taylor & Francis, 2010.
[16] E.S. Gawlik, F. Gay-Balmaz, A finite element method for MHD that preserves energy, cross-helicity, magnetic helicity, incompressibility, and $\mathrm{div} \cdot \boldsymbol{B} = 0$, J. Comput. Phys. 450 (2022) 110847.
[17] E. Hairer, C. Lubich, G. Wanner, Geometric Numerical Integration: Structure-Preserving Algorithms for Ordinary Differential Equations, vol. 31, Springer Science & Business Media, 2006.
[18] J. Kreeft, A. Palha, M. Gerritsma, Mimetic framework on curvilinear quadrilaterals of arbitrary order, arXiv:1111.4304, 2011, p. 69.
[19] Y. Zhang, Mimetic spectral element method and extensions toward higher computational efficiency, 2022.
[20] P. Knupp, S. Steinberg, Fundamentals of Grid Generation, CRC Press, 2020.
[21] B. Sanderse, Energy-conserving Runge–Kutta methods for the incompressible Navier–Stokes equations, J. Comput. Phys. 233 (2013) 100–131.
[22] H. Clercx, C.-H. Bruneau, The normal and oblique collision of a dipole with a no-slip boundary, Comput. Fluids 35 (3) (2006) 245–279.
[23] O. Botella, R. Peyret, Benchmark spectral results on the lid-driven cavity flow, Comput. Fluids 27 (4) (1998) 421–433.
[24] G.H. Golub, J.H. Welsch, Calculation of Gauss quadrature rules, Math. Comput. 23 (106) (1969) 221–230.